

Full length article

On the mechanism of {332} twinning in metastable β titanium alloysM.J. Lai^{**}, C.C. Tasan^{*}, D. Raabe

Max-Planck-Institut für Eisenforschung GmbH, Max-Planck-Str. 1, 40237 Düsseldorf, Germany

ARTICLE INFO

Article history:

Received 25 December 2015

Received in revised form

11 March 2016

Accepted 12 March 2016

Keywords:

 β titanium

Deformation twinning

Martensitic transformation

Electron backscatter diffraction

Transmission electron microscopy

ABSTRACT

{332} twinning, an unusual twinning mode in other body-centered cubic (bcc) metals and alloys, has been demonstrated to be a fundamental deformation mode in bcc metastable β titanium alloys. Recent studies suggest that this twinning mode plays an important role in enhancing the work hardening and thus improving the mechanical properties. Here, we studied the mechanism of this twinning mode in a metastable β Ti–36Nb–2Ta–3Zr (wt.%) alloy. Tensile tests were performed to induce the formation of {332} twins. By using electron backscatter diffraction, transmission electron microscopy and in situ scanning electron microscopy, the surface-to-bulk microstructures and the initiation and propagation of {332} twins were investigated. In addition to the previously reported high densities of straight dislocations within the twin, we have observed that an α'' martensite band is present near the surface adjacent to the twin. During annealing at 900 °C, the α'' martensite band transforms into the adjacent twin rather than into the matrix, indicating that {332} twin nucleates within α'' martensite. Further evidence for this is the constitution of the twin in the initial stage of its formation, where the first portion formed consists of α'' martensite. During propagation, the twins propagating to the opposite directions can merge together when their lateral boundaries impinge on each other. Based on the experimental observations, an α'' -assisted twinning mechanism is proposed and the origin of the dislocations within {332} twin is discussed accordingly.

© 2016 Published by Elsevier Ltd on behalf of Acta Materialia Inc.

1. Introduction

In addition to dislocation slip, deformation twinning is another fundamental plastic deformation mode in crystalline solids [1]. In materials with low crystal symmetry such as hexagonal close-packed (hcp) metals and some nanoscale metals, twinning even dominates the plastic deformation [1–3]. In materials with high crystal symmetry such as face-centered cubic (fcc) and body-centered cubic (bcc) metals, where dislocation slip commonly prevails, deformation twinning is also of high relevance, since the twin boundaries that progressively form with increasing strain are effective obstacles to gliding dislocations [4–6]. This means that deformation twinning provides a substantial work hardening mechanism (twinning-induced plasticity (TWIP) effect) for these materials. Thus, the introduction of deformation twinning, e.g., by tailoring the stacking fault energy in fcc TWIP steels [7], has become an important approach for enhancing both strength and

ductility.

Recently, the deformation mechanisms in bcc β titanium alloys have been studied in more detail, especially in so-called multifunctional β titanium alloys (e.g., gum metal), primarily due to their considerable potential for biomedical applications and their unusual gum-like deformation behavior [8,9]. It was found that dislocation slip dominates the plastic deformation in stable β titanium alloys, while reduced bcc β phase stability results in the activation of additional deformation mechanisms including {112} <111> twinning, {332}<113> twinning and stress-induced α'' martensitic transformation [10–15]. Thus, like the stacking fault energy in fcc alloys, the β phase stability can serve as a criterion for the introduction of deformation twinning in bcc β titanium alloys. Hanada and Izumi [16] investigated the correlation of tensile properties, deformation mechanisms and phase stability in a series of β titanium alloys and found that the {332}<113> twinning associated with low β phase stability produced a high work hardening rate and thus significantly improved the poor ductility involved in slip-dominated β titanium alloys. Min et al. [17,18] suggested that a combination of dislocation slip and {332}<113> twinning was effective for achieving high yield strength and large uniform elongation. These improvements in mechanical properties

* Corresponding author.

** Corresponding author.

E-mail addresses: m.lai@mpie.de (M.J. Lai), c.tasan@mpie.de (C.C. Tasan).

linked with TWIP effect, resembling those in TWIP steels [7], have attracted much attention recently in the design of metastable β titanium alloys with high strength and good ductility [19–21].

In bcc metals and alloys, $\{112\}\langle 111\rangle$ is the most common twinning mode and is believed to form by the collective glide of partial dislocations (twinning dislocations) with the same Burgers vector $1/6\langle 111\rangle$ on successive $\{112\}$ crystallographic planes [1,3]. By contrast, $\{332\}\langle 113\rangle$ twinning is much less common and had long been known as a unique twinning mode for metastable β titanium alloys since its first identification in a Ti–11.5Mo–6Zr–4.5Sn (wt.%) alloy in 1971 [22]. Recently, this twinning mode has been observed in shock-loaded bcc α -Fe and α -Fe alloys [23,24]. A common characteristic of materials where $\{332\}\langle 113\rangle$ twinning occurs is that all of them are subjected to diffusionless phase transformations during water quenching or deformation, such as the $\beta \rightarrow \omega$ (bcc \rightarrow hexagonal or trigonal) or $\beta \rightarrow \alpha''$ (bcc \rightarrow orthorhombic) transitions in metastable Ti–Mo-based alloys [16,19–22,25–27], Ti–Nb-based alloys [25,26,28], Ti–V-based alloys [15,16,25,26,29], Ti–Cr alloys [30] and Ti–Fe alloys [25] and the $\alpha \rightarrow \varepsilon$ (bcc \rightarrow hcp) transition in shock-loaded α -Fe and α -Fe alloys [23,24]. Both twinning and diffusionless phase transformations involve shear processes, but their interrelationship is not yet clear.

Earlier reports [16,22,25–27,29] suggest that the internal microstructure of $\{332\}\langle 113\rangle$ twins is characteristic of either a high density of dislocations or stress-induced ω plates depending on β phase stability. In alloys with higher β phase stability, high densities of parallel straight dislocations have been observed traversing the $\{332\}\langle 113\rangle$ twins [16,22,25–27,29]. These straight dislocations in some circumstances seem to penetrate through the twin/matrix interface, extending into the β -matrix [16,27,29]. Furuhara et al. [29] speculated that the dislocations on the β -matrix side extending from $\{332\}\langle 113\rangle$ twins might be expelled from the twin/matrix interface during the shrinkage of twins upon unloading. In alloys with lower β phase stability, it was reported that one particular ω variant within the $\{332\}\langle 113\rangle$ twins was preferentially induced, producing a series of parallel ω plates of the same variant, which even evolved to occupy the whole twinned domain and caused the twinned region to become a single-variant ω plate with further decreasing β phase stability [25,26,29]. These internal dislocations or ω plates should render twinned regions harder than the matrix and should, therefore, contribute to the high work hardening rate associated with $\{332\}\langle 113\rangle$ twinning [16–18,26].

Crocker [31] proposed the first crystallographic model for the mechanism of $\{332\}\langle 113\rangle$ twinning. He illustrated that simple shears on successive twinning planes along the twinning direction such as that in $\{112\}\langle 111\rangle$ twinning could only move one half of the atoms from the untwinned lattice sites to their correct twinned lattice sites, so that additional shuffles were necessary for the other half of the atoms to reach their twinned positions. This shear mechanism involves large shuffles on planes with a small interplanar spacing [31], which may be energetically difficult. Therefore, several attempts have been made to overcome this problem, including the proposal of partial dislocation mechanisms [32–35] and a modification of Crocker's shear mechanism [36]. Kawabata et al. [32] suggested that $\{332\}\langle 113\rangle$ twinning could be accomplished by successive slip of $1/22\langle 113\rangle$ partial dislocations on pairs of neighboring $\{332\}$ planes and subsequent shuffle of these paired planes towards each other along the $\pm\langle 332\rangle$ directions. A similar partial dislocation mechanism was also present in the work by Litvinov and Rusakov [33], where they proposed an additional partial dislocation mechanism characterized by the glide of $5/22\langle 113\rangle$ partial dislocations on a stack of $\{332\}$ planes without any additional atomic shuffle. Since neither the $\{332\}$ plane nor the $\langle 113\rangle$ direction is close-packed, the question whether such partial

dislocation mechanisms are energetically favorable remains open. Recently, Tobe et al. [36] modified Crocker's shear mechanism by considering the instable bcc β lattice (characterized by the shuffling of adjacent $\{0\bar{1}1\}$ planes to $\langle 011\rangle$ directions) as a modulated structure with base-centered tetragonal symmetry, producing a new shear mechanism with a smaller shuffling magnitude compared to Crocker's mechanism. It should be noted that both the partial dislocation mechanisms and the shear mechanisms can generate an ideal $\{332\}\langle 113\rangle$ twin lattice, but none of them has reasonably accounted for the characteristic internal microstructures (i.e., straight dislocations or ω plates) of $\{332\}\langle 113\rangle$ twins.

The present study has the aim of improving the understanding of the mechanism of $\{332\}$ twinning. A metastable β Ti–36Nb–2Ta–3Zr (wt.%) alloy was produced by arc melting and drop casting. We performed tensile tests to induce the formation of $\{332\}$ twins and then characterized the surface-to-bulk microstructures of these twins using scanning electron microscopy (SEM), electron backscatter diffraction (EBSD), transmission electron microscopy (TEM) and synchrotron X-ray diffraction (SXRD). The evolution of these twins during high-temperature annealing was also examined. The initiation and propagation of these twins were studied by conducting in situ SEM experiments.

2. Experimental

The metastable β titanium alloy used in this study was produced by arc-melting mixed elemental materials with a target composition of Ti–36Nb–2Ta–3Zr (wt.%) under argon atmosphere and drop casting into a copper mold with an internal dimension of $10 \times 60 \text{ mm}^2$. In order to promote chemical homogeneity, the as-cast ingot was homogenized at $1200 \text{ }^\circ\text{C}$ for 4 h, under vacuum, followed by furnace cooling. After that, it was sealed in a vacuum quartz tube, annealed at $1000 \text{ }^\circ\text{C}$ for 1 h and water quenched. The microstructure of the as-quenched alloy consists of large equiaxed grains with an average size of $\sim 1000 \text{ }\mu\text{m}$ and its measured chemical composition is Ti–35.7Nb–2.01Ta–2.98Zr–0.07O (wt.%). In order to maintain the large grain size for better observation of the evolution of deformation microstructures, the as-quenched alloy was not subjected to any hot- or cold-working before the following tailored deformation experiments.

Flat dog-bone-shaped tensile samples with a gauge section length of 4 mm and a cross section of $2 \times 1 \text{ mm}^2$ were cut using electrical discharge machining (EDM). Prior to tensile deformation, one of their two $4 \times 2 \text{ mm}^2$ surfaces was polished for microstructural characterization and the other one was painted with a graphite speckle pattern for digital image correlation analysis [37]. These samples were then deformed to an engineering strain of $\sim 6.5\%$ on a Kammrath and Weiss (Dortmund, Germany) tensile stage with an initial strain rate of $5 \times 10^{-4} \text{ s}^{-1}$. Backscattered electron (BSE) imaging and EBSD mapping were performed to characterize the deformation microstructures on the pre-polished surface, after which the deformed samples were held at $900 \text{ }^\circ\text{C}$ for 30 min under vacuum followed by fast cooling. The cooling rate was estimated to be $\sim 200 \text{ }^\circ\text{C/s}$. These heat treatments were carried out using a Baehr Dil805 dilatometer. The heat-treated samples were subjected to EBSD mapping again on the same surface without any additional grinding or polishing.

For investigating the evolution of the deformation microstructure with accumulating strain, additional dog-bone-shaped tensile samples with gauge section dimension of $4 \times 1 \times 0.5 \text{ mm}^2$ were cut using EDM. One $4 \times 1 \text{ mm}^2$ surface of these samples was polished prior to deformation. They were then deformed on an in situ tensile stage mounted in a scanning electron microscope. The tensile tests were conducted at a constant cross head speed $2 \text{ }\mu\text{m/s}$ (corresponding to an initial strain rate of $5 \times 10^{-4} \text{ s}^{-1}$) and were

interrupted at various strain levels for microstructural observation on the pre-polished surface.

The experimental route for characterizing the deformation-induced microstructures is schematically shown in Fig. 1a. All SEM observations and EBSD mapping were performed in a Zeiss-Crossbeam XB 1540 FIB-SEM instrument (Carl Zeiss SMT AG, Germany) operated at 15 kV. The EBSD data were collected by an EDAX/TSL data acquisition system (Draper, UT, USA) and automatically indexed by the standard vote-rank algorithm [38]. SXRD experiments were carried out on beam-line P02.1 at PETRA III (DESY Hamburg, Germany) using 60 keV X-rays with a wavelength of 0.20727 Å. The Fit2D software [39] was used to calibrate the raw two-dimensional diffraction patterns and to output the intensity/ 2θ spectra. TEM lamellae were cut from the pre-polished surface by using a dual-beam focused ion beam (FIB) workstation (FEI Helios Nanolab 600). The intersection of deformation-induced microstructure features such as slip bands and twins with the pre-polished surface resulted in surface roughness, which enabled the identification and site-specific FIB cutting of specific microstructure features from locations of interest. An example is shown in Fig. 1b, where the in-depth TEM lamella contains a portion of the bulk of the deformation band. This lamella was then lifted out by a manipulator, welded to a copper grid and milled to become electron-transparent. Before FIB cutting, a Pt layer with a thickness of $\sim 4 \mu\text{m}$ was deposited on the surface to protect the lamella. TEM observations were conducted in a JEOL JEM-2200FS microscope operated at 200 kV.

3. Results

3.1. Surface-to-bulk characterization of {332} twins

Prior to deformation, the as-quenched Ti–36Nb–2Ta–3Zr alloy consisted of large β grains with an average grain size of $\sim 1000 \mu\text{m}$, as shown by the EBSD inverse pole figure (IPF) map in Fig. 2a. The colors on the IPF map represent the crystallographic orientation normal to the observed plane as indicated by the color bar on the right hand side of Fig. 2a. Neither twins nor secondary phases have been detected by EBSD. Nonetheless, weak and elongated diffraction spots from hexagonal ω phase have been observed by using TEM, similar to the situation in other as-quenched metastable β titanium alloys [25,40]. Representative deformation microstructures on the pre-polished surface of the tensile samples are shown

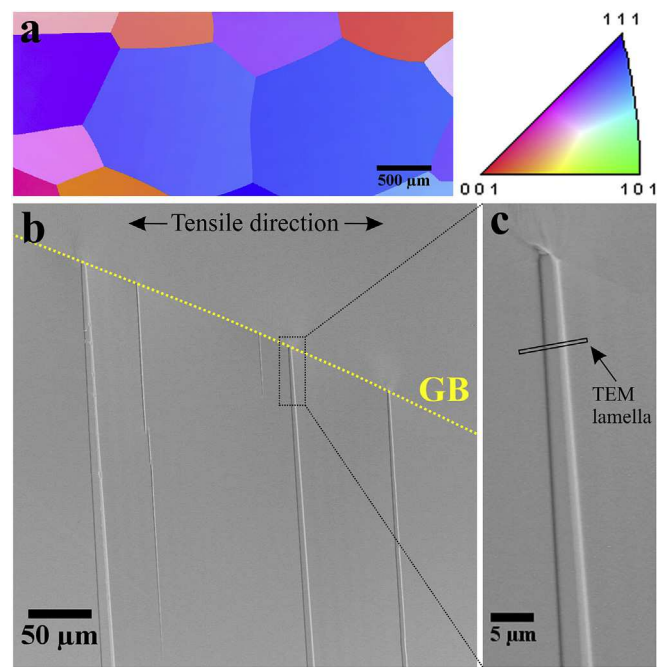


Fig. 2. Pre- and post-deformation microstructures on the polished surface of the tensile samples. (a) Inverse pole figure map of the pre-deformation microstructure. The color bar is shown as a stereographic triangle on the right hand side. (b) Back-scattered electron image of the post-deformation microstructure. The yellow dashed line indicates a grain boundary (GB). (c) An image of the boxed region in (b) taken at a higher magnification. The small rectangle indicates the location for preparing in-depth TEM lamella by FIB. (For interpretation of the references to color in this figure legend, the reader is referred to the web version of this article.)

in Fig. 2b, which are characteristic of nearly straight deformation bands with width ranging from $<1 \mu\text{m}$ to tens of micrometers. Closer observation (Fig. 2c) reveals that the deformation band is composed of two parts along its length, which exhibit different contrasts in the BSE image.

Fig. 3 shows the EBSD analysis of the area highlighted in Fig. 2c. The entire deformation band has been indexed as bcc β phase by EBSD with an average confidence index value above 90%. The two portions of the deformation band along its length exhibit two slightly different colors on the IPF map (Fig. 3a), corresponding to

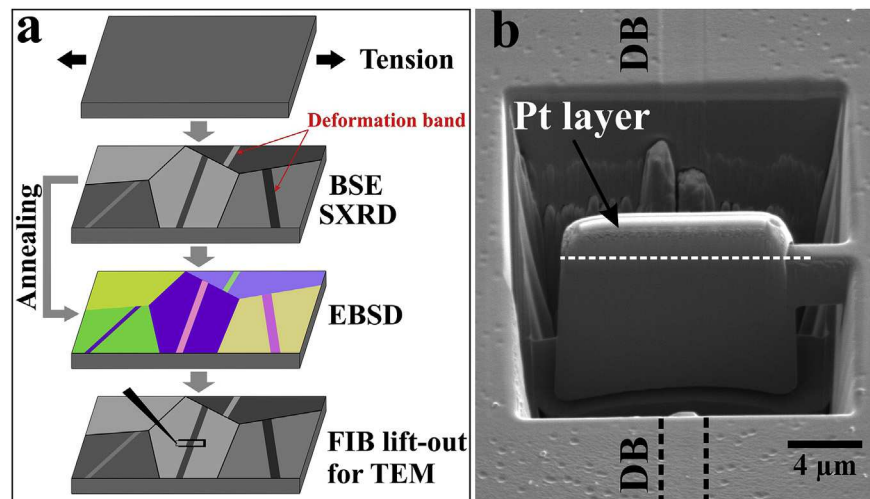


Fig. 1. (a) Experimental route for characterization. (b) Example of an in-depth TEM lamella cut from a deformation band (DB).

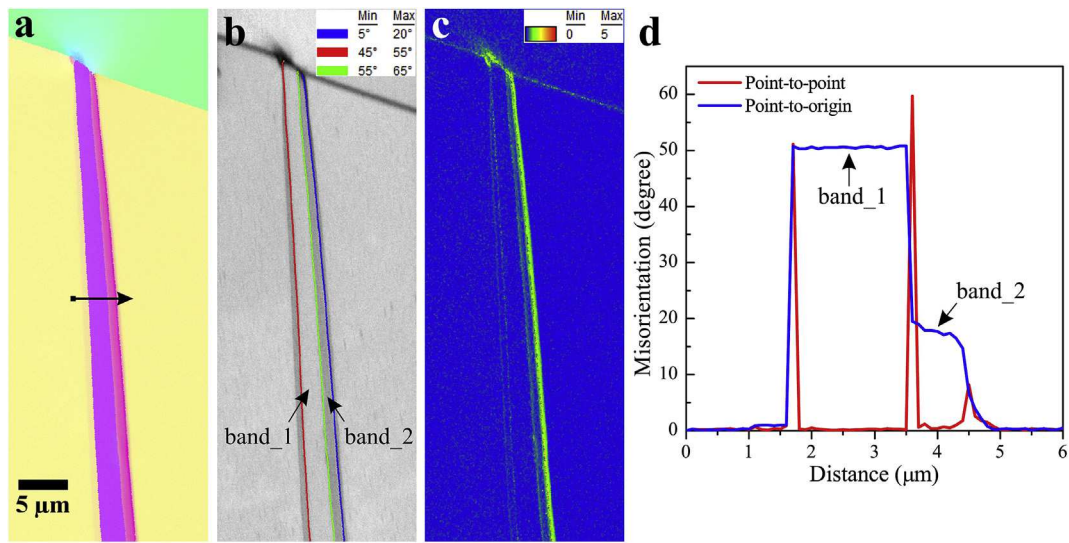


Fig. 3. EBSD analysis of the deformation band shown in Fig. 2c. (a) Inverse pole figure map. The color bar is the same as that in Fig. 2a. (b) Image quality map superimposed with rotation angle boundaries (blue, red and green lines). (c) Kernel average misorientation map. (d) Misorientation profile along the arrow in (a). (For interpretation of the references to color in this figure legend, the reader is referred to the web version of this article.)

different crystallographic orientations. This means that the deformation band shown in Fig. 2c is indeed composed of two bands which are closely adjacent to each other. Hereafter, the bands on the left and right hand sides will be referred to as band_1 and band_2, respectively, as indicated in Fig. 3b. Fig. 3d displays the point-to-point and point-to-origin misorientation profiles along the arrow in Fig. 3a. The two bands form two plateaus in the point-to-origin misorientation profile. The point-to-point misorientation angle across the matrix/band_1 boundary is 51.1° , corresponding to the $\{332\}\langle 113\rangle$ twinning system, while that across the band_1/band_2 boundary is 59.7° , corresponding to the $\{112\}\langle 111\rangle$ twinning system [41]. An abrupt change occurs in the point-to-origin misorientation profile when crossing these two boundaries. Such an abrupt change is, however, absent for the band_2/matrix boundary. The point-to-origin misorientation angle across this boundary gradually decreases along the distance between $4.3\ \mu\text{m}$ and $4.9\ \mu\text{m}$ instead. The image quality (IQ) map (Fig. 3b) superimposed with these boundaries shows that there is a layer on the matrix side adjacent to the matrix/band_1 boundary, which also generates a plateau with a relatively small misorientation angle ($\sim 1^\circ$) in the point-to-origin misorientation profile (Fig. 3d). All of the boundaries are clearly visualized on the kernel average misorientation (KAM) map (Fig. 3c), where the KAM value represents the density of geometrically necessary dislocation (GND). The band_2/matrix boundary is visualized as a layer with a width of about $0.6\ \mu\text{m}$. The higher KAM value of this layer than that of the matrix suggests that high densities of GNDs are stored within it, interpreting the above mentioned gradual change of point-to-origin misorientation angle.

The deformation bands were characterized in greater detail by using TEM analysis, where the bulk microstructures of the deformation bands were revealed. Fig. 4 displays the TEM analysis of a FIB lift-out lamella prepared from the location indicated in Fig. 2c. Fig. 4a is a scanning transmission electron microscope (STEM) bright-field image, illustrating a lower magnification overview of the deformation band. It is shown that band_1 penetrates considerably deep into the bulk, while band_2 is located near the surface with its largest depth reaching down to $\sim 450\ \text{nm}$. The twinning relationship between matrix and band_1 was confirmed by selected area diffraction (SAD) patterns (Fig. 4c, d and f). Following

the usual notation for deformation twinning, a twin can be described by four elements: twinning plane K_1 , twinning direction η_1 , conjugate twinning plane K_2 and conjugate twinning direction η_2 [42]. The SAD pattern (Fig. 4f) taken from the band_1/matrix boundary and its key diagram (Fig. 4i) imply that the twinning plane K_1 is $(\bar{2}33)$. Zhang et al. [43] proposed a theoretical method to calculate the other twinning elements with K_1 as input. By applying this method to the present twin (band_1), the η_1 , K_2 and η_2 are determined to be $[311]$, (211) and $[\bar{1}11]$, respectively. The SAD pattern in Fig. 4e demonstrates that band_2 consists of an orthorhombic α'' martensite phase rather than a bcc β phase, in contrast to the EBSD indexing (Fig. 3). The cross section of the α'' band is nearly triangle-shaped and locates on the β -twin side (Fig. 4a and b). The α''/β -matrix boundary is characterized by a series of wrinkles emitted from the triple point of β -twin, α'' martensite and β -matrix (Fig. 4b), which align along the straight extension of the β -twin/ β -matrix boundary. These wrinkles may be created by stress concentrations along the boundary, consistent with the high densities of GNDs indicated by the KAM map (Fig. 3c).

Elongated ω reflections are present in the SAD patterns of both β -matrix (Fig. 4c) and β -twin (Fig. 4d). In the β -matrix, the four ω variants (referred to as ω_1 , ω_2 , ω_3 and ω_4), with $[2110]_{\omega_1}$, $[\bar{1}014]_{\omega_2}$, $[01\bar{1}4]_{\omega_3}$ and $[\bar{1}2\bar{1}0]_{\omega_4}$ parallel to $[0\bar{1}1]$, precipitated with equal probability during quenching, so the diffraction intensities of the two distinguishable ω variants (ω_1 and ω_4) are identical [11]. Within the β -twin, however, the intensity of ω_4 is stronger than that of ω_1 , indicating that more ω_4 formed during twinning. The orientation relationship between β -twin and ω_4 is $[01\bar{1}]_{\text{T}}//[\bar{1}2\bar{1}0]_{\omega_4}$, $[\bar{1}11]_{\text{T}}//[0001]_{\omega_4}$ and $(211)_{\text{T}}/(\bar{1}010)_{\omega_4}$, where the subscript “T” represents the β -twin.¹ Fig. 4g illustrates that the reflections of ω_4 further intensify near the β -twin/ α'' boundary. In a previous work [11], we have demonstrated that $\{211\}\langle 111\rangle$ shear in β phase can induce $\beta \rightarrow \omega$ transformation. This means that $(211)_{\text{T}}[\bar{1}11]_{\text{T}}$ shear was involved within the β -twin, especially near the β -twin/ α'' boundary, during the formation of β -twin. The orientation relationship between β -twin and α'' martensite, as determined from the SAD pattern in Fig. 4g and its key diagram in

¹ The indices without any subscript are with respect to the β -matrix in this paper.

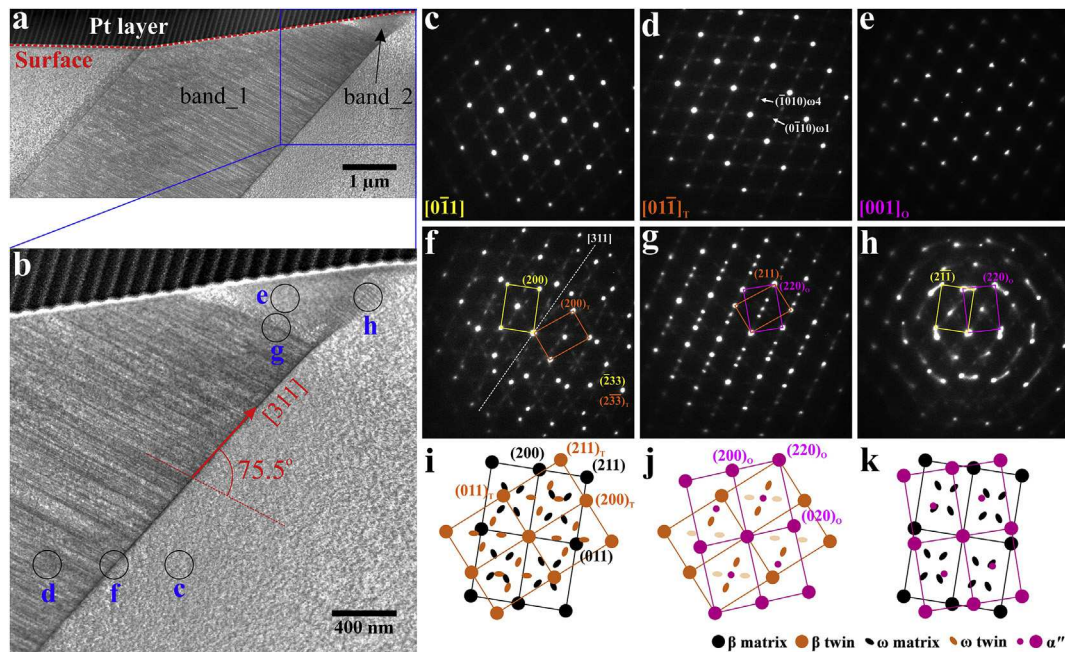


Fig. 4. TEM analysis of a FIB lift-out lamella prepared from the location indicated in Fig. 2c. (a) STEM bright-field image of the deformation band viewed along $[0\bar{1}1]$. (b) An image of the boxed region in (a) taken at a higher magnification. (c–h) SAD patterns taken from the regions indicated by circles in (b). (i–k) Key diagrams corresponding to the SAD patterns in (f), (g) and (h), respectively. The indices in the bottom left corner of (c), (d) and (e) indicate the corresponding zone axes. The subscripts “T” and “O” denote bcc β -twin and orthorhombic α' , respectively.

Fig. 4j, is $[0\bar{1}1]_T/[001]_O$, $[1\bar{1}1]_T/[1\bar{1}0]_O$ and $(211)_T/(110)_O$, where the subscript “O” represents the orthorhombic α' martensite. The $[001]_O/[0\bar{1}1]_T$ SAD pattern taken from the wrinkled boundary between the α' martensite and the β -matrix shows circular streaks between the two set of reflections (Fig. 4h and k), where the α' reflections seem to be dragged to their current sites from locations close to the β -matrix reflections with a tail formed following each α' reflection. It is illustrated that $(110)_O$ is about 14.3° deviated from (211) .

Like previous studies [16,22,25–27,29], high densities of straightly elongated dislocations are present within the $\{233\}$ twin (Fig. 4a and b). The dislocation lines are nearly parallel to the $(211)_T$ and $(110)_O$ planes. The angle between the dislocation lines and the $[311]$ direction (β -twin boundary) is about 75.5° (Fig. 4b). These dislocations seem to penetrate through the β -twin/ β -matrix interface on the left hand side of Fig. 4a and extend into the β -matrix, producing a layer along the interface which corresponds to the layer adjacent to the red boundary (45° – 55°) on the IQ map (Fig. 3b) and the plateau of $\sim 1^\circ$ in Fig. 3d. Such dislocation-decorated layers in the vicinity of $\{332\}$ twins were previously reported in other metastable β titanium alloys as well, e.g., in Ti–Mo-based and Ti–V-based alloys [16,27,29].

In order to characterize the Burgers vector of the dislocations within the $\{332\}$ twins, TEM lamellae with orientations close to $\langle 111 \rangle_T$ were prepared and tilting experiments and contrast analyses were performed, as shown in Fig. 5. A β -twin with width $6.69 \mu\text{m}$ is indicated in Fig. 5a, where a triangle-shaped α' region is also present on the β -twin side near the surface (inset). The straightly elongated dislocations in this twin seem to penetrate through the β -twin/ β -matrix interface and extend into the β -matrix as well. Fig. 5b, c and d present three typical STEM bright-field images of the same area surrounding the β -twin/ β -matrix interface taken at $\mathbf{g} = (101)_T$, $\mathbf{g} = (110)_T$ and $\mathbf{g} = (01\bar{1})_T$, respectively. It is seen that the dislocations are visible under the former two two-beam diffraction conditions but invisible under the last one. This

means that the straight dislocations within the twin are of the same Burgers vector \mathbf{b} . Using $\mathbf{g} \cdot \mathbf{b} = 0$ as the criterion for invisibility, the Burgers vector \mathbf{b} is determined to be $1/2[111]_T$, which is nearly parallel ($\sim 4.5^\circ$ deviation) to the dislocation lines. Thus, these straight dislocations have a very strong screw character.

The atomic configurations of the β -matrix/ β -twin interface have been examined by using high resolution TEM (HRTEM). Fig. 6a is the HRTEM image of a $\{233\}$ twin, which shows that the lattice fringes of β -matrix and β -twin are symmetrical with respect to the β -matrix/ β -twin interface (or twinning plane), where the interface is parallel to the incident electron beam. The fast Fourier transform (FFT) image in Fig. 6b reveals how the lattices of the β -matrix (yellow) and the β -twin (origin) are rotated about the $[0\bar{1}1]_T/[0\bar{1}1]_T$ crystallographic axis. The angle between (011) and $(011)_T$ lattice fringes is about 50.5° , as indicated in Fig. 6a. Thus, the β -twin lattice can be derived from the β -matrix lattice by a 50.5° rotation around $[0\bar{1}1]_T$, consistent with the misorientation determined by EBSD (Fig. 3d). Within the coincidence site lattice (CSL) description, such an interface forms a $\Sigma 11$ boundary. The magnified HRTEM micrograph of the β -matrix/ β -twin interface is illustrated in Fig. 6c, where the $\Sigma 11$ boundary is indicated by a blue line and two $\{233\}/\{233\}_T$ atomic planes close to the boundary are marked by open circles. A nearly coherent interface is revealed. It should be noted that the interface is not flat at the atomic scale and the (011) and $(011)_T$ lattice fringes close to the interface are not straight, implying crystal distortions near the interface.

The lattice parameters of the β and α' phases were determined by SXRD experiments, where SXRD patterns were taken from the deformed regions of the tensile samples and intensity $^{1/2}/2\theta$ spectra were extracted from these patterns. Fig. 7 displays such an intensity $^{1/2}/2\theta$ spectrum, which shows distinct peaks derived from both bcc β phase (Space group: $\text{Im}\bar{3}\text{m}$) and orthorhombic α' martensite (space group: Cmcm). The fitted lattice parameter of the β phase is $a_\beta = 3.2949 \text{ \AA}$, while that of the α' martensite is $a_0 = 3.2196 \text{ \AA}$, $b_0 = 4.7676 \text{ \AA}$ and $c_0 = 4.6417 \text{ \AA}$.

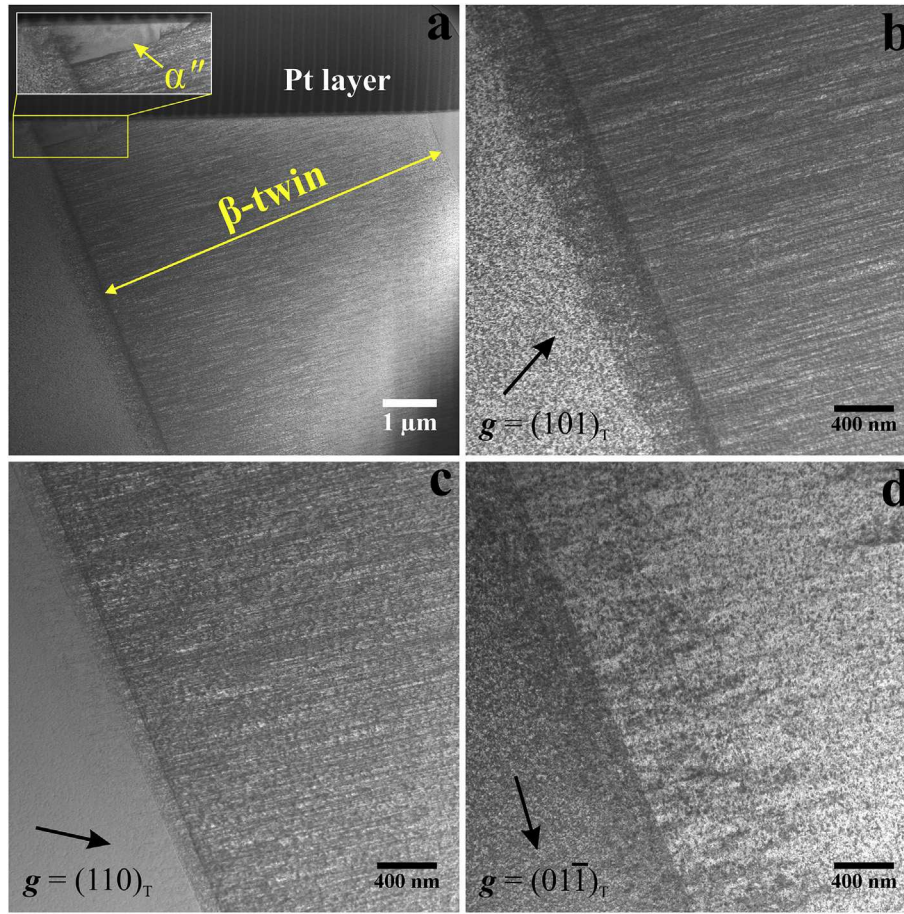


Fig. 5. Contrast analysis of the dislocations within the {332} twin. (a) STEM bright-field image of a β -twin captured in a FIB lift-out TEM lamella. The inset shows the α'' region near the surface at a higher magnification. (b–d) STEM bright-field images of the same area surrounding the β -twin/ β -matrix interface taken under different two-beam diffraction conditions. g is diffraction vector.

The α'' crystal lattice can be derived from the β crystal lattice by $\{0\bar{1}1\}\langle 011\rangle$ shuffles with a relatively small shuffle amplitude δ [44,45], as schematically illustrated in Fig. 8a. The lattice parameters of the α'' martensite, a_o , b_o and c_o , correspond to a_β , $\sqrt{2}a_\beta$ and $\sqrt{2}a_\beta$, respectively. The shuffling process is normally accompanied by a shape change which can be described by three principal transformation strains:

$$\varepsilon_1 = (a_o - a_\beta) / a_\beta, \quad (1a)$$

$$\varepsilon_2 = (b_o - \sqrt{2}a_\beta) / \sqrt{2}a_\beta, \quad (1b)$$

$$\varepsilon_3 = (c_o - \sqrt{2}a_\beta) / \sqrt{2}a_\beta. \quad (1c)$$

The substitution of the lattice parameters measured by SXRD into the above equations gives $\varepsilon_1 = -2.29\%$, $\varepsilon_2 = 2.32\%$ and $\varepsilon_3 = -0.39\%$ for the current Ti–36Nb–2Ta–3Zr alloy. These small strain values correspond to a very small shape change, i.e., the α'' crystal lattice is close to the β crystal lattice, resulting in that the EBSD Kikuchi patterns of α'' exhibit a pseudo-cubic symmetry. Therefore, the β and α'' phases cannot be unambiguously discriminated by EBSD indexing with the standard vote-rank algorithm [38]. An example is illustrated in Fig. 8b, which shows that an EBSD Kikuchi pattern taken from the α'' martensite can be indexed as both bcc β and orthorhombic α'' with almost the same number of

votes. This explains why the entire deformation band could be indexed as β phase with a high confidence index value in Fig. 3. It should be noted that we can still distinguish the {332} twin and the α'' martensite by examining misorientations, although they were indexed as the same phase by EBSD.

3.2. Initiation and propagation of {332} twins

The occurrence of α'' martensite bands adjacent to the {332} twins near the free surface indicates an intimate relationship between {332} twinning and $\beta \rightarrow \alpha''$ transformation. In order to clarify this relationship, the initiation and propagation of {332} twins have been investigated. In most cases, the {332} twin nucleates at a grain boundary. Fig. 9 shows such a case, where a deformation band has nucleated at one grain boundary and has then propagated into the grain interior with a length of 48 μm . The width of this band decreases gradually from its initiation site to its tip, tapering to a point in the end (Fig. 9a). The IPF map in Fig. 9b illustrates that the color of this band is not homogeneous along its length, indicating varied crystallographic orientations. By examining misorientations and plotting the rotation angle boundaries onto the IQ map (Fig. 9c), it is revealed that this band is not purely composed of {332} twin. In Fig. 9c, as revealed in the previous subsection, the blue line ($5-20^\circ$), red line ($45-55^\circ$) and green line ($55-65^\circ$) correspond to β -matrix/ α'' boundary, β -matrix/ β -twin boundary and α'' / β -twin boundary, respectively. Thus, starting from its initiation site at the grain boundary, this band along its length is

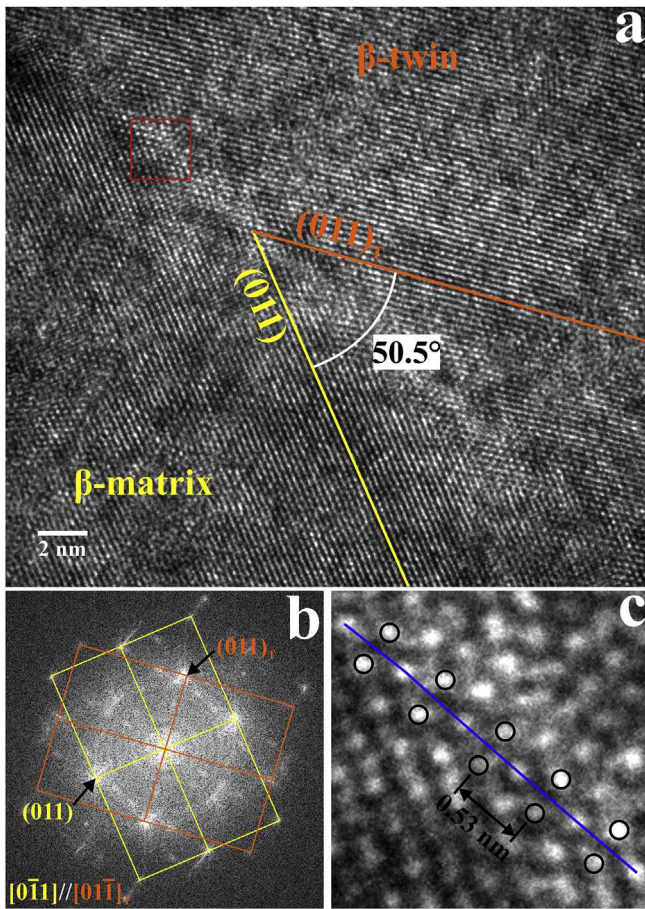


Fig. 6. Atomic scale characterization of the β -matrix/ β -twin interface. (a) HRTEM image of the β -matrix/ β -twin interface viewed along $[0\bar{1}1]//[01\bar{1}]_{\beta}$. (b) Fast Fourier transform pattern of (a). (c) Magnified image of the boxed region in (a). The blue line indicates the β -matrix/ β -twin interface, while the black open circles indicate two $\{233\} // \{2\bar{3}\bar{3}\}_{\beta}$ atomic planes close to the interface (a detailed atomic model is shown below in Fig. 14b). (For interpretation of the references to color in this figure legend, the reader is referred to the web version of this article.)

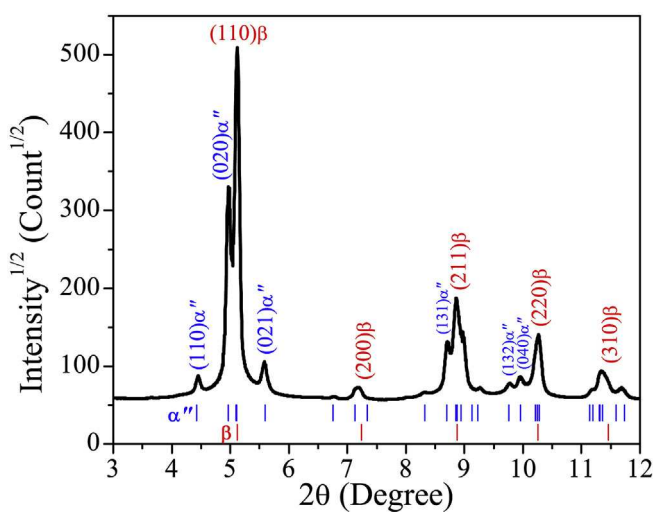


Fig. 7. Intensity^{1/2}/20 spectrum extracted from the SXRD pattern taken from the deformed region of a tensile sample. The positions of the β and α'' peaks are labeled and indexed.

composed of α''/β -twin/ α''/β -twin in sequence, which seems to imply that α'' band formed first and β -twin initiated within the α'' band. The intermittent α'' and β -twin sections along the band length can also be visualized on the KAM map (Fig. 9d), with β -matrix/ α'' boundaries exhibiting higher KAM values (consistent with that revealed in Fig. 3c). It should be noted that $\{332\}$ twin nucleates in the grain interior as well, forming a lenticular shape, as displayed in Fig. 2b.

Fig. 10 and the Supplementary Movie show the results of an in situ SEM tensile test conducted on a pre-polished tensile sample, where the propagation of $\{332\}$ twins with accumulating strain is illustrated. The engineering tensile stress curve is presented in Fig. 10a as a function of the ratio of the cross head displacement ΔL over the initial gauge length L_0 . The applied strain levels at which BSE images (Fig. 10b–f) were taken are marked in this curve. Fig. 10b shows two twins propagating to the opposite directions. With the increase of applied strain, jerky formation of new twins accompanied by drops in the engineering stress was observed, as presented in the BSE images of Fig. 10c–f. These images also reveal that the growth of initiated twins is characterized by expanding in the longitudinal direction and thickening in the transverse direction, identical to the growth of conventional $\{112\}\langle 111 \rangle$ twins in bcc metals [3]. Another interesting feature revealed by these images is that the twins propagating to the opposite directions can merge when their lateral boundaries impinge on each other. This feature has been studied in more detail by correlating higher-magnification BSE images (Fig. 10g–i) and EBSD maps (Fig. 11) below.

Supplementary data related to this article can be found online at <http://dx.doi.org/10.1016/j.actamat.2016.03.040>.

Fig. 11 displays the IPF map and IQ map of the twins shown in Fig. 10f. By examining misorientations (Fig. 11b), we can determine that the purple, pink and blue colors on the IPF map (Fig. 11a) correspond to β -matrix, β -twin and α'' martensite, respectively. It is shown that each twin is accompanied by an α'' martensite band on its left hand side. By correlating the EBSD analysis to the BSE images, the merging process of adjacent twins is shown in more detail in Fig. 10g–i. Two twins are labeled in Fig. 10g as β -twin_1 and β -twin_2, respectively, where the former is a pure twin and the latter is accompanied by an α'' martensite band along its length. The TEM analyses (Figs. 4 and 5) in the previous subsection have revealed that the α'' martensite locates near the free surface (beneath the α'' martensite is the β -twin) and the α''/β -matrix boundary is oriented along the straight extension of the β -twin/ β -matrix boundary, i.e., the α''/β -matrix boundary in Fig. 10g corresponds to the left boundary of β -twin_2. With increasing the applied strain, β -twin_1 and β -twin_2 grew by consuming adjacent β -matrix and eventually merged when their lateral boundaries impinged on each other (Figs. 10h and 11). During this process, an α'' martensite band accompanying β -twin_1 formed on its left hand side. Also shown in Fig. 10h is the propagation of another twin (labeled β -twin_3) into the field of view. With further increasing the applied strain, Fig. 10i illustrates that the β -matrix in the field of view was completely consumed and β -twin_3 merged with β -twin_1, i.e., the three twins in the field of view coalesced into a single twin in this stage. Interestingly, the α'' martensite bands remained unchanged during the merging of twins.

3.3. Evolution of α'' martensite and $\{332\}$ twins during annealing

It is well known that α'' martensite will transform into the β phase when holding the sample at high temperatures, depending of course on the specific alloy composition [46]. In the present work, the α'' martensite bands occurring near the surface are in contact with both the β -matrix and the $\{332\}$ β -twins. The question that

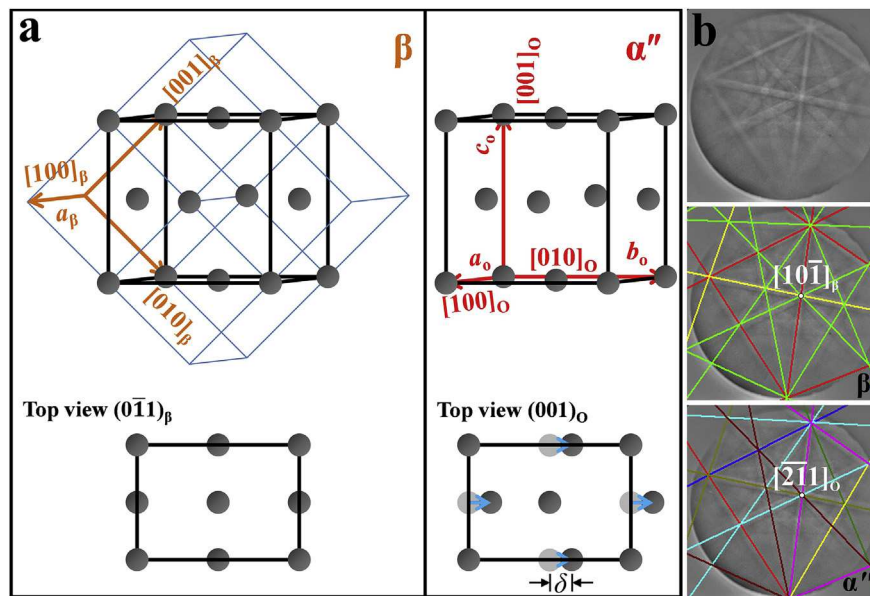


Fig. 8. (a) Lattice correspondence between bcc β phase and orthorhombic α'' martensite. (b) EBSD Kikuchi pattern taken from the α'' martensite on the pre-polished surface of a tensile sample, which can be indexed as both β and α'' .

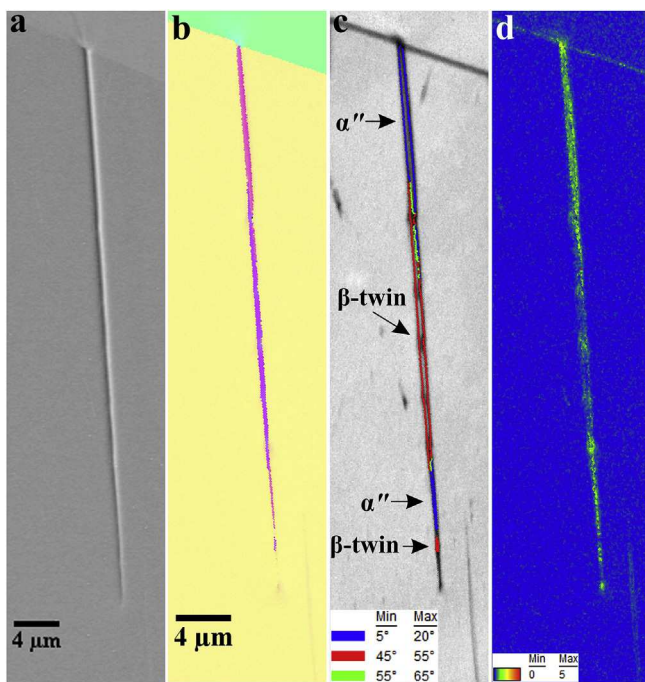


Fig. 9. Initiation of $\{332\}$ twin at grain boundary. (a) Backscattered electron image, (b) inverse pole figure map, (c) image quality map overlaid with rotation angle boundaries (blue, red and green lines) and (d) kernel average misorientation map of the same region. The color bar of (b) is the same as that of Fig. 2a. (For interpretation of the references to color in this figure legend, the reader is referred to the web version of this article.)

arises is what the α'' martensite band will transform to during high-temperature annealing, β -matrix or β -twin. It is of importance to clarify this question for determining the relationship between α'' martensitic transformation and $\{332\}$ twinning.

Fig. 12a and b show the IPF map and IQ map of a $\{332\}$ β -twin with an α'' martensite band adjacent to it, as confirmed by the rotation angles of the boundaries overlaid in Fig. 12b. Viewed on the

surface, the width of the α'' martensite is about three times that of the β -twin. The same region was mapped again by EBSD after annealing at 900 °C for 30 min, without any grinding or polishing on the surface. It is revealed that the α'' martensite band has completely transformed into the β -twin rather than into the β -matrix (Fig. 12c and d). This suggests that α'' martensite acts as initiation site of the β -twin.

Another interesting phenomenon is that detwinning of $\{332\}$ twins occurred during annealing, as shown in Fig. 13. The IQ map in Fig. 13a displays the traces of four twins existed before annealing, which are marked as T1, T2, T3 and T4, respectively. T1, T2 and T3 are parallel, indicating that they belong to the same twinning variant [41]. T4 which belongs to another twinning variant intersected with them. The widths of T1 and T2 taper when they approaching T4, indicating that they initiated elsewhere and propagated to T4. In contrast, T3 seems to nucleate from T4. The line features inside T4 may result from merging processes of twins as revealed in the previous subsection. The IPF map in Fig. 13b and the rotation angle boundaries overlaid in Fig. 13a illustrate that T1 fully detwinned, while T2 and T4 partially detwinned. The detwinning process starts from the twin tip rather than the initiation site or lateral boundaries of the twin, as manifested by T2 and T3. This is different from the reversion of martensite band which starts from its lateral boundaries [47].

4. Discussion

Experimental observations of the present study illustrate the three-dimensional microstructure of $\{332\}$ twin in a metastable β Ti–36Nb–2Ta–3Zr alloy. In addition to the parallel straight dislocations inside the twin which have been reported previously [16,22,25–27,29], we found that an α'' martensite band with triangle-shaped cross section was embedded in the $\{332\}$ twin near the surface. Combine the surface EBSD analysis in Fig. 3 with the through-thickness TEM analysis in Fig. 4, we can schematically rebuild the three-dimensional microstructure of the $\{332\}$ twin shown in Fig. 2c, as displayed in Fig. 14a. The $(\bar{2}33)$ twin viewed on the $(0\bar{1}1)$ plane was inclined to the horizontal at an angle of $\theta_1 = 48.74 \pm 0.18^\circ$ and produced an inclined plane at an angle of

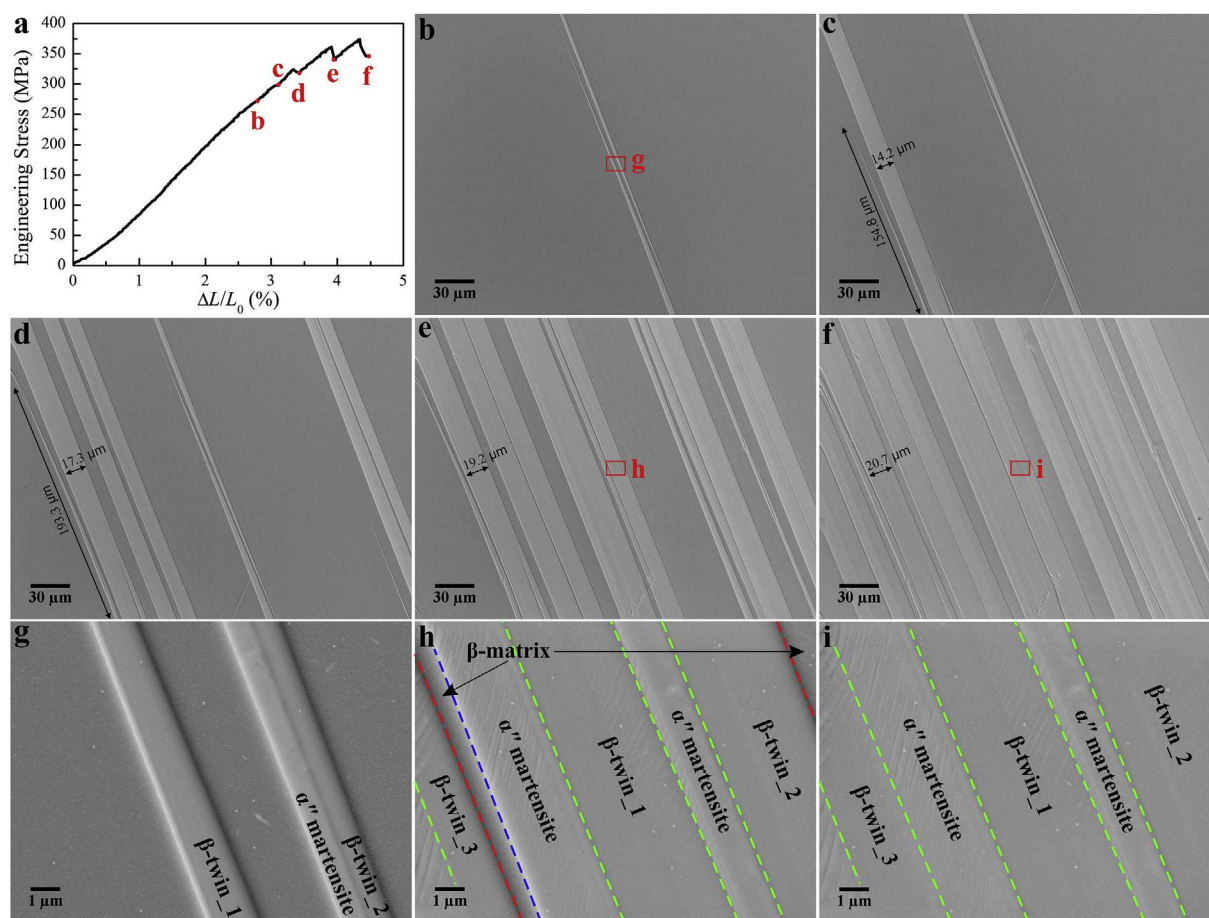


Fig. 10. Propagation of {332} twins with accumulating strain. (a) Engineering stress against the ratio of the cross head displacement ΔL over the initial gauge length L_0 . (b–f) Sequential backscattered electron images showing the propagation of {332} twins at the strain levels indicated in (a). The tensile direction is horizontal with respect to the image. (g–i) Images of the boxed regions in (b), (e) and (f), respectively, taken at a higher magnification. The red, green and blue dashed lines denote β -twin/ β -matrix boundary, β -twin/ α' boundary and α' / β -matrix boundary, respectively. (For interpretation of the references to color in this figure legend, the reader is referred to the web version of this article.)

$\theta_2 = 7.66 \pm 0.16^\circ$ when it intersected the surface as measured in Fig. 4a. With these two inclination angles, the shear strain s' generated by the twin can be calculated as

$$s' = \frac{\sin \theta_2}{\sin \theta_1 \sin(\theta_1 - \theta_2)} = 0.2697. \quad (2)$$

The details for the derivation of the above equation are presented as [Supplementary online material](#).

Fig. 14b schematically shows a projection of twinned crystal structures onto the $(0\bar{1}1)$ plane as observed via HRTEM studies (Fig. 6). The K_1 and K_2 planes and η_1 and η_2 directions are illustrated with respect to the β -matrix. The plane perpendicular to K_1 and K_2 , i.e., the $(0\bar{1}1)$ plane, is called the plane of shear. According to the theory of the crystallography of deformation twinning [42], the inclination angle θ_2 (Fig. 14a) produced by twinning shear reaches its maximum when the twin is viewed on the plane of shear. This explains why the angle θ_2 in Fig. 5a is fairly small ($\sim 0^\circ$), where the twin was not viewed on the plane of shear. The shear mechanisms [31,36] and partial dislocation mechanisms [32–35] proposed for {332} twinning are generally characterized by two activities, i.e., (i) collective movement of atoms on successive {332} planes along $\langle 113 \rangle$ directions and (ii) additional atomic shuffles, with the macroscopic shear strain merely contributed by the former activity. All of these mechanisms give a shear strain (magnitude of twinning shear) $s = 0.3536$ [31,32,36], which is larger than the

experimentally measured shear strain $s' = 0.2697$. Indeed, the shear strain produced by deformation twinning is strongly dependent on the twinning mechanism. For instance, recent studies [48,49] suggest that some special twinning mechanisms even result in zero net shear strain for the conventional fcc {111} twinning mode. Here, the discrepancy between s and s' implies that {332} twinning may not involve the movement of atoms on successive {332} planes along $\langle 113 \rangle$ directions as claimed in the shear mechanisms [31,36] and partial dislocation mechanisms [32–35]. The enrichment of one ω variant within the twin (ω_4 , Fig. 4d and g), on the other hand, suggests that {332} twinning involves the shear of $\langle 211 \rangle_T$ planes along $\langle \bar{1}11 \rangle_T$ directions.

Based on the fact that the α' martensite band near the surface transformed into the adjacent β -twin rather than into the β -matrix during annealing (Fig. 12), we propose here that the {332} twin nucleates within the progressively formed α' martensite during deformation, i.e., the stress-induced α' martensite forms first and then transforms to the {332} twin. This scenario is supported by Fig. 9, which clearly shows that the α' martensite first initiated from a grain boundary and the {332} twin formed within the α' martensite. Such an α' -assisted twinning mechanism also explains why the α' / β -matrix and β -twin/ β -matrix boundaries are almost aligned along the same line (Figs. 4a and 5a). In order to better understand this mechanism, we first consider the nature of the $\beta \rightarrow \alpha'$ martensitic transformation in the metastable β Ti–36Nb–2Ta–3Zr alloy by employing the phenomenological theory of

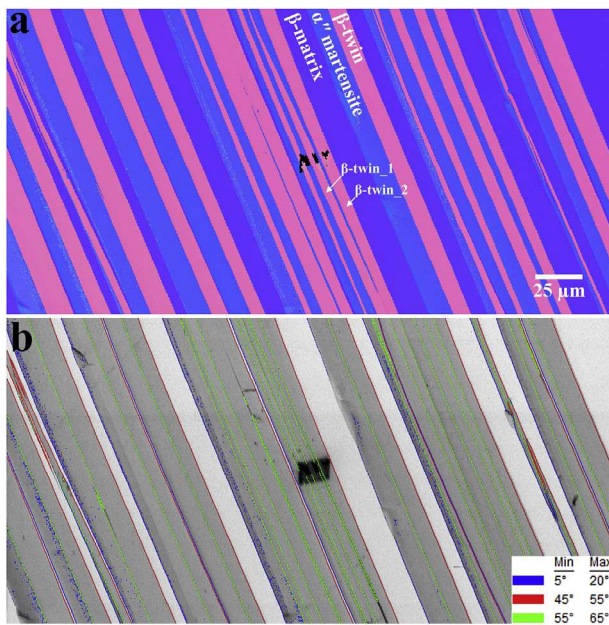


Fig. 11. EBSD analysis of the twins shown in Fig. 10f: (a) inverse pole figure map and (b) image quality map superimposed with rotation angle boundaries (blue, red and green lines). The color bar of (a) is the same as that of Fig. 2a. The areas of poor indexing in the center of the two maps, represented as black pixels, result from electron beam-induced contamination yielded by continuous high-magnification imaging. (For interpretation of the references to color in this figure legend, the reader is referred to the web version of this article.)

martensitic transformations (PTMT) as outlined by Lieberman et al. [50].

When the bcc β phase transforms into the orthorhombic α'' martensite, the difference in their crystal structures generates large amounts of local strain. Normally, this strain is accommodated by producing a twinned martensite structure on a lattice invariant plane (habit plane) of the β phase. The relative amounts of the two twin-related variants, x and $(1 - x)$, the habit plane and the orientation relationships can be predicted by PTMT with the lattice parameters and twinning relationship as inputs. The orthorhombic α'' martensite has six crystallographic variants (designated as V1, V2, V3, V4, V5 and V6), which may be twin-related to each other via $\{111\}_0$ type I twinning, $\langle 211 \rangle_0$ type II twinning or $\{011\}_0$ compound twinning when forming in the β -matrix, as illustrated in Fig. 15. By applying the infinitesimal deformation approach by Liang et al. [51] to the $\beta \rightarrow \alpha''$ transformation, Inamura et al. [52] proposed that the twinning relationship amongst the α'' variants is dependent on the sign of ϵ_3 , where $\epsilon_3 > 0$ corresponds to type I or type II twinning and $\epsilon_3 < 0$ corresponds to compound twinning. For the present Ti–36Nb–2Ta–3Zr alloy, the ϵ_3 component as determined by SXR is -0.39% , implying a compound twinning relationship.

When applying PTMT to the present $\beta \rightarrow \alpha''$ transformation, we consider the two α'' variants, V1 and V2, shown in Fig. 15 and use the lattice parameters which were measured by SXR experiments. Table 1 lists the calculated crystallographic characteristics of the transformation, where x is the relative amount of V1, \mathbf{n} the normal of the habit plane, \mathbf{s} the direction of shear, \mathbf{t} the transformation twinning plane (between V1 and V2), m the magnitude of shear and

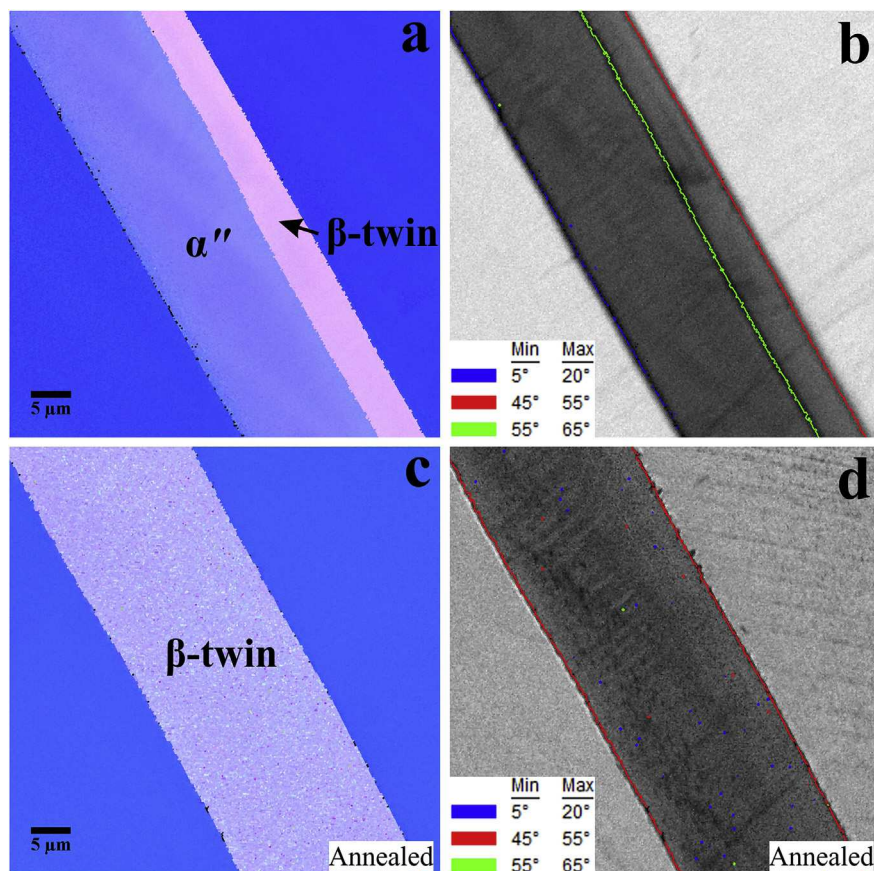


Fig. 12. EBSD analysis of a $\{332\}$ twin before (a, b) and after (c, d) annealing at 900°C for 30 min. (a, c) Inverse pole figure map. The color bar is the same as that of Fig. 2a. (b, d) Image quality map superimposed with rotation angle boundaries (blue, red and green lines). (For interpretation of the references to color in this figure legend, the reader is referred to the web version of this article.)

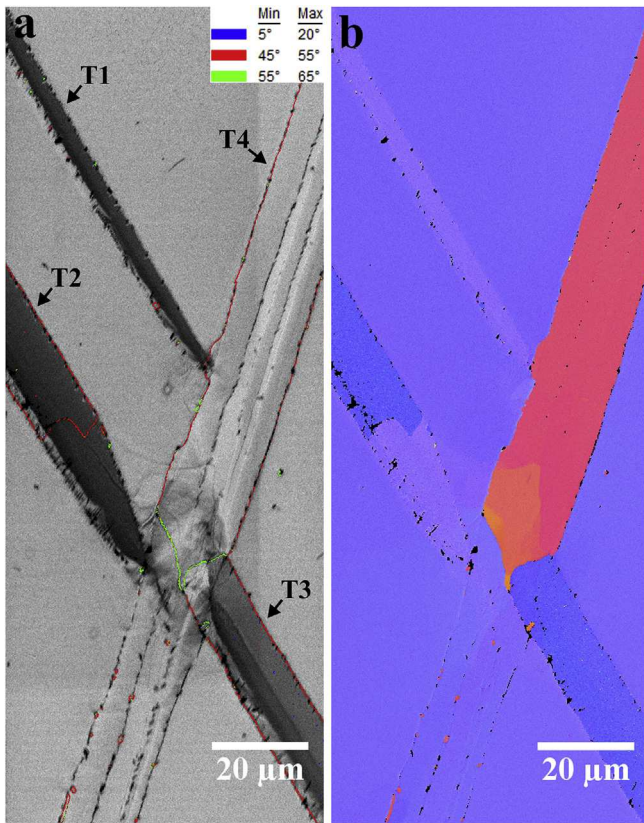


Fig. 13. Detwinning of $\{332\}$ twins after annealing at 900 C for 30 min. (a) Image quality map superimposed with rotation angle boundaries (blue, red and green lines). (b) Inverse pole figure map. The color bar is the same as that of Fig. 2a. (For interpretation of the references to color in this figure legend, the reader is referred to the web version of this article.)

θ the angle of shear. The table shows that the indices of both habit plane and transformation twinning plane are irrational with respect to the coordinate system of the β -matrix, implying that these interfaces may be semi-coherent or incoherent. Such interfaces are normally characteristic of terraces and steps and are stabilized by the presence of dislocations, as revealed by Chai et al. [53] in a series of metastable β Ti–Nb alloys with Nb content ranging from 20 to 24 at.%. When viewed edge-on along the $[001]_{\alpha''} \parallel [010]_{\alpha''} \parallel [010]_{\alpha'} \parallel [010]_{\beta}$ direction, they showed that the V2/V1 interface relaxed into a series of $(110)_0$ terraces and steps.

The rotation matrices Θ and Ω defining the orientation relationships between the β -matrix and the martensite variants V1 and V2, respectively, are calculated to be

$$\Theta = \begin{pmatrix} 0.9998 & -0.0149 & 0.0148 \\ 0.0006 & 0.7231 & 0.6907 \\ -0.0210 & -0.6906 & 0.7230 \end{pmatrix} \quad (3a)$$

and

$$\Omega = \begin{pmatrix} -0.9998 & 0.0149 & -0.0148 \\ -0.0210 & -0.7097 & 0.7042 \\ 0.0000 & 0.7044 & 0.7098 \end{pmatrix}. \quad (3b)$$

With these two rotation matrices, any vector expressed with respect to the coordinate system of the β -matrix can be transformed into the same vector expressed with respect to the coordinate systems of the martensite variants. Table 2 lists the orientation relationships between important crystallographic

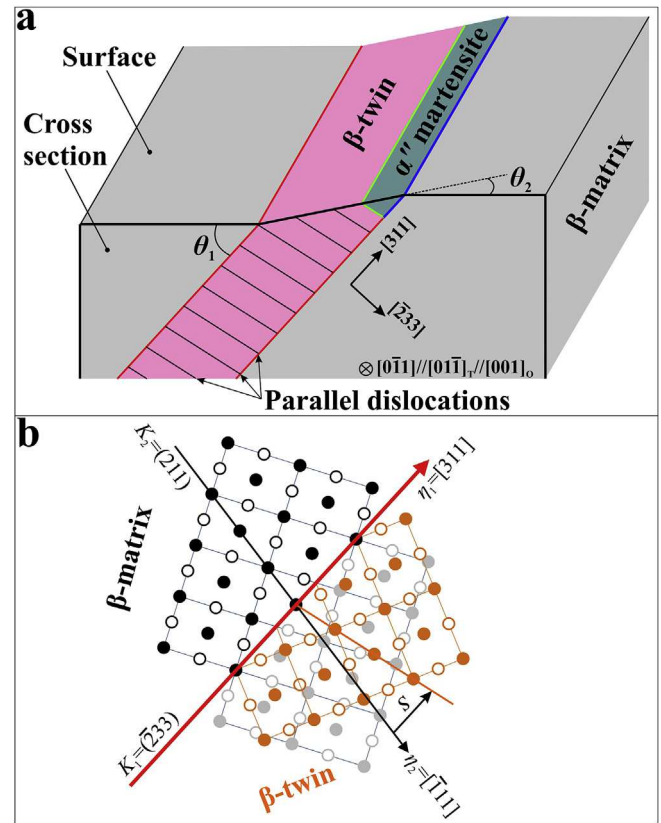


Fig. 14. Schematic illustrations of the $(\bar{2}33)$ twin. (a) Three-dimensional illustration the $(\bar{2}33)$ twin shown in Fig. 2c rebuilt by the EBSD analysis in Fig. 3 and TEM analysis in Fig. 4. (b) Atomic model of the twinned crystal structures. The solid circles indicate the atoms on plane of figure, while the open circles the atoms below plane of figure.

planes predicted by PTMT. The angles between these planes are fairly small, indicating relatively small differences in the $\langle 0\bar{1}1 \rangle // \langle 001 \rangle_0$ SAD patterns, i.e., the reflections of the α'' martensite are close to those of the β -matrix at the onset of the formation of α'' martensite. Both reduction in temperature and application of stress can act as driving forces for the $\beta \rightarrow \alpha''$ martensitic transformation. For the former case, it has been revealed that the SAD pattern of the α'' martensite is close to that of the β -matrix when taken along $[001]_0 // [0\bar{1}1]$ in water quenched Ti–Nb alloys [53], analogous to the prediction. Nonetheless, few studies have been conducted to examine the orientation relationship between the initially formed α'' martensite and the β -matrix for the latter case, which may be due to the difficulty in retaining such martensite.

Under an external biasing stress, the initially formed twinned martensite during deformation will reorient and detwin [54], resulting in a single-variant martensite structure with a new orientation relationship relative to the β -matrix. This may explain the single-variant character and special orientation of the α'' martensite band observed in the present study, which was retained after tensile deformation (Fig. 4). The possible scenario is that twin-related α'' martensite variants formed first and then detwinned into one single variant and reoriented with respect to the β -matrix. The wrinkled microstructures which were observed to form along the α''/β -matrix boundary in Fig. 4b (corresponding to high KAM values, Fig. 3c) and the circular diffraction streaks (or tails following the α'' reflections) in Fig. 4h may thus result from the reorientation of the α'' martensite. These circular streaks starting from the locations close to the β -matrix reflections seem to indicate that the $\langle 001 \rangle_0$ SAD patterns of the initially formed α'' martensite variants

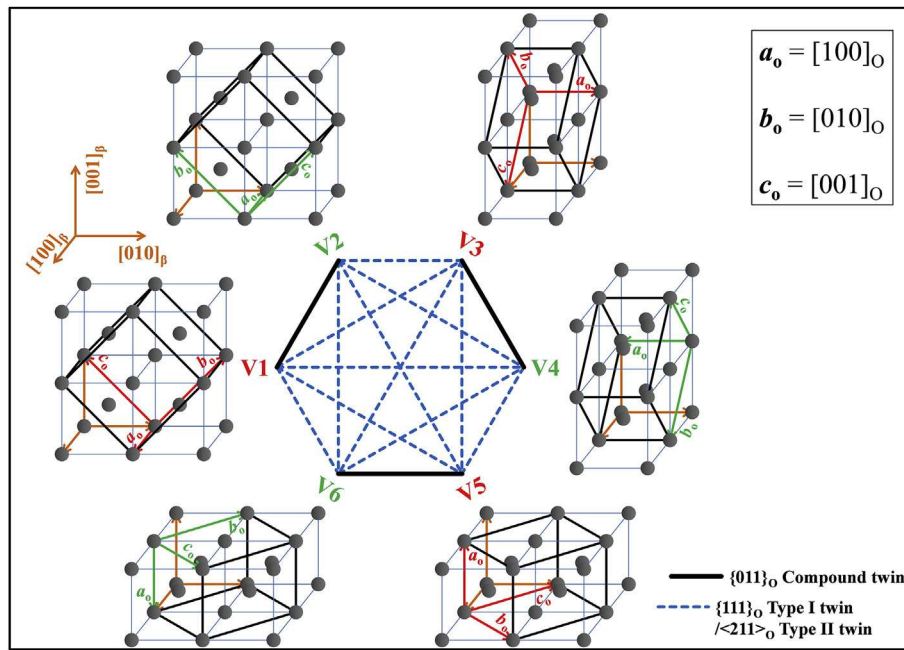


Fig. 15. Lattice correspondence between bcc β phase and six orthorhombic α'' martensite variants.

Table 1
Crystallographic characteristics of the $\beta \rightarrow \alpha''$ transformation in the Ti–36Nb–2Ta–3Zr alloy calculated by the phenomenological theory of martensitic transformations [50]. All of the vectors are with respect to the coordinate system of the β -matrix.

x	n	s	t	m	θ
0.8554	$\begin{pmatrix} 0.7336 \\ -0.4828 \\ 0.4783 \end{pmatrix}$	$\begin{pmatrix} 0.6796 \\ 0.5211 \\ -0.5163 \end{pmatrix}$	$\begin{pmatrix} -0.0205 \\ -0.6907 \\ 0.6909 \end{pmatrix}$	0.0463	2.4069°

Table 2
Orientation relationships between β -matrix and two α'' martensite variants, V1 and V2, calculated by the phenomenological theory of martensitic transformations [50].

β and V1	β and V2
(100) 1.20° from (100) _{V1}	($\bar{1}00$) 1.20° from (100) _{V2}
(011) 1.31° from (010) _{V1}	(0 $\bar{1}1$) 1.22° from (010) _{V2}
(0 $\bar{1}1$) 1.78° from (001) _{V1}	(011) 0.22° from (001) _{V2}
(211) 1.25° from (110) _{V1}	($\bar{2}11$) 0.14° from (110) _{V2}
($\bar{2}11$) 2.16° from ($\bar{1}10$) _{V1}	($\bar{2}11$) 2.46° from ($\bar{1}10$) _{V2}

during deformation are close to the [0 $\bar{1}1$] SAD pattern of the β -matrix as predicted by the PTMT. After the detwinning and reorientation, the (110)_O plane of the resultant single-variant α'' martensite is nearly parallel to the (211)_T plane of the β -twin (Fig. 4g).

As revealed in Fig. 12, the detwinned and reoriented α'' martensite transformed back into bcc β phase during high-temperature annealing, but the resultant β domain was of a {332} twinning relationship relative to the β -matrix. We assume that the $\alpha'' \rightarrow \beta$ transformation can be induced by the application of external stress as well, resulting in the formation of β -twins within the detwinned and reoriented α'' martensite as shown in Fig. 9. This transformation should have involved atomic shears parallel to the $\langle 0001 \rangle_{\omega}$ direction of one of the four ω variants ($\{211\}_{T} \langle \bar{1}11 \rangle_{T}$ shears), similar to the $\beta \rightarrow \alpha''$ transformation [11], thus leading to the preferential growth (or enrichment) of this specific ω variant within the β -twin (Fig. 4d and g). It should be noted that the β -twin may initiate from different positions of the same α'' martensite

band (Fig. 9c) and these initiated β -twins can merge together when they propagate to each other as revealed in Fig. 10. Theoretical studies [55,56] suggested that the presence of free surface stabilizes the martensite. In the present study, the retained α'' martensite near the surface has only been observed on the side of the β -twin where the angle between the β -twin/ β -matrix interface (parallel to the α'' / β -matrix interface) and surface is acute. Such a geometrical feature may resist the $\alpha'' \rightarrow \beta$ transformation and thus stabilizes the α'' martensite.

The dislocations contributing to the (110)_O terraces and steps of the V2/V1 interface in the initially formed twinned martensite structure may be retained after the detwinning of martensite. These dislocations, lying on the {110}_O planes of the resultant single-variant martensite, would then become parallel to the {211}_T planes after the reorientation of martensite and may be left behind in the β -twin after the $\alpha'' \rightarrow \beta$ transformation (reverse martensitic transformation). This provides a possible explanation for the origin of the straight parallel dislocations within the {332} twins, which were found to be almost parallel to the (110)_O and (211)_T planes (Fig. 4b). Similar phenomena have been reported by Kajiwara and Kikuchi [47,57], where dislocation structures produced in parent phase by reverse martensitic transformation were observed in Cu–Zn and Fe–Ni–C alloys and they suggested that such dislocations originated from the twinning dislocations at the interfaces of martensite twins. For the dislocations on the matrix side which seem to be extended from the dislocations inside the β -twin (Figs. 4 and 5), Furuhashi et al. [29] suggested that they originated from the reverse motion of β -matrix/ β -twin interface during detwinning. However, we found that the detwinning of {332} twins started from

their twin tips rather than from their lateral coherent twin boundaries (Fig. 13). In fact, the coherent twin boundaries have been considered to be very stable against migration due to their fairly low excess energy [58]. Thus, we suggest that the dislocations on the matrix side originated from the reverse transformation of the α'' martensite which was not yet subjected to reorientation. Such martensite transformed to the β domain with the same orientation as the β -matrix during unloading, while the dislocations lying on the $\{110\}_O$ planes were left behind after the transformation.

5. Conclusions

The mechanism of $\{332\}$ twinning has been studied in a metastable β Ti–36Nb–2Ta–3Zr alloy. We conducted tensile tests to induce the formation of $\{332\}$ β -twins and then characterized the surface-to-bulk microstructures of these β -twins using SEM, EBSD, TEM and SXRD. The initiation and propagation of the β -twins were investigated by performing in situ SEM experiments. In addition, the evolution of the β -twins during annealing was examined by using EBSD analysis. Based on the experimental observations, we draw the following conclusions:

- Near the surface, an α'' martensite band with triangle-shaped cross section is embedded in the β -twin. The β -twin/ β -matrix boundary and the α'' / β -matrix boundary are oriented almost along the same line. The orientation relationship between β -twin and α'' is $[01\bar{1}]_T//[001]_O$, $[1\bar{1}\bar{1}]_T//[1\bar{1}0]_O$ and $(211)_T//(110)_O$ (the subscripts “T” and “O” represent β -twin and α'' , respectively), while a regular orientation relationship is absent between β -matrix and α'' .
- High densities of straight parallel dislocations are present within the β -twin. These dislocations are of a very strong screw character and all have the same Burgers vector, $1/2\langle\bar{1}11\rangle_T$. One ω variant is enriched within the β -twin. The macroscopic shear strain produced by the β -twin is smaller than that predicted by the classic theory of the crystallography of deformation twinning.
- The β -twin/ β -matrix interface is nearly coherent. The shape changes in crystal structures associated with the $\beta \rightarrow \alpha''$ transformation are relatively small, but the α'' martensite, β -twin and β -matrix on the surface can be distinguished by examining misorientations in EBSD analysis.
- The β -twins initiate both at the grain boundaries and in the grain interiors. The first initiated band consists of α'' martensite and the β -twin forms within the α'' martensite. The β -twins propagating to the opposite directions can merge when their lateral boundaries impinge on each other, but the α'' martensite bands near the surface remain unchanged during the merging processes.
- The $\alpha'' \rightarrow \beta$ transformation and detwinning of β -twins occur during annealing at 900 °C. The α'' martensite band near the surface transforms into the adjacent β -twin rather than into the β -matrix, while the detwinning of β -twin starts from the twin tip rather than from the lateral twin boundaries.
- An α'' -assisted twinning mechanism is proposed, in which $\{332\}$ twins nucleate within progressively formed α'' martensite during deformation. Explanations for the enrichment of one ω variant and the occurrence of straight dislocations within the β -twin are given based on this mechanism.

Acknowledgments

M.J.L. would like to thank China Scholarship Council for the scholarship granted to support this work. The authors would like to

thank J.-L. Zhang and D.S. Yan for their help in heat treatment and in situ SEM experiments. Dr. J.J. Li and Dr. A. Evirgen are gratefully appreciated by M.J.L. for fruitful discussions. The funding from the European Research Council under the EU's 7th Framework Programme (FP7/2007–2013)/ERC Grant Agreement No. 290998 is gratefully acknowledged.

Appendix A. Supplementary data

Supplementary data related to this article can be found at <http://dx.doi.org/10.1016/j.actamat.2016.03.040>.

References

- [1] J.W. Christian, S. Mahajan, Deformation twinning, *Prog. Mater. Sci.* 39 (1995) 1–157.
- [2] Y.T. Zhu, X.Z. Liao, X.L. Wu, Deformation twinning in nanocrystalline materials, *Prog. Mater. Sci.* 57 (2012) 1–62.
- [3] J. Wang, Z. Zeng, C.R. Weinberger, Z. Zhang, T. Zhu, S.X. Mao, In situ atomic-scale observation of twinning-dominated deformation in nanoscale body-centred cubic tungsten, *Nat. Mater.* 14 (2015) 594–600.
- [4] O. Bouaziz, N. Guelton, Modelling of TWIP effect on work-hardening, *Mater. Sci. Eng. A* 319–321 (2001) 246–249.
- [5] D.R. Steinmetz, T. Jäpel, B. Wietbrock, P. Eisenlohr, I. Gutierrez-Urrutia, A. Saeed-Akbari, T. Hickel, F. Roters, D. Raabe, Revealing the strain-hardening behavior of twinning-induced plasticity steels: theory, simulations, experiments, *Acta Mater.* 61 (2013) 494–510.
- [6] I. Gutierrez-Urrutia, D. Raabe, Dislocation and twin substructure evolution during strain hardening of an Fe–22 wt.% Mn–0.6 wt.% C TWIP steel observed by electron channeling contrast imaging, *Acta Mater.* 59 (2011) 6449–6462.
- [7] O. Bouaziz, S. Allain, C.P. Scott, P. Cugy, D. Barbier, High manganese austenitic twinning induced plasticity steels: a review of the microstructure properties relationships, *Curr. Opin. Solid State Mater. Sci.* 15 (2011) 141–168.
- [8] T. Saito, T. Furuta, J.H. Hwang, S. Kuramoto, K. Nishino, N. Suzuki, R. Chen, A. Yamada, K. Ito, Y. Seno, T. Nonaka, H. Ikehata, N. Nagasako, C. Iwamoto, Y. Ikuhara, T. Sakuma, Multifunctional alloys obtained via a dislocation-free plastic deformation mechanism, *Science* 300 (2003) 464–467.
- [9] Y.L. Hao, S.J. Li, B.B. Sun, M.L. Sui, R. Yang, Ductile titanium alloy with low Poisson's ratio, *Phys. Rev. Lett.* 98 (2007).
- [10] M.J. Lai, C.C. Tasan, D. Raabe, Deformation mechanism of ω -enriched Ti–Nb-based gum metal: dislocation channeling and deformation induced ω - β transformation, *Acta Mater.* 100 (2015) 290–300.
- [11] M.J. Lai, C.C. Tasan, J. Zhang, B. Grabowski, L.F. Huang, D. Raabe, Origin of shear induced β to ω transition in Ti–Nb-based alloys, *Acta Mater.* 92 (2015) 55–63.
- [12] Y. Yang, G.P. Li, G.M. Cheng, Y.L. Li, K. Yang, Multiple deformation mechanisms of Ti–22.4Nb–0.73Ta–2.0Zr–1.340 alloy, *Appl. Phys. Lett.* 94 (2009) 061901.
- [13] Y. Yang, G.P. Li, G.M. Cheng, H. Wang, M. Zhang, F. Xu, K. Yang, Stress-introduced α'' martensite and twinning in a multifunctional titanium alloy, *Scr. Mater.* 58 (2008) 9–12.
- [14] Y. Yang, S.Q. Wu, G.P. Li, Y.L. Li, Y.F. Lu, K. Yang, P. Ge, Evolution of deformation mechanisms of Ti–22.4Nb–0.73Ta–2Zr–1.340 alloy during straining, *Acta Mater.* 58 (2010) 2778–2787.
- [15] M. Ahmed, D. Wexler, G. Casillas, O.M. Ivasishin, E.V. Pereloma, The influence of β phase stability on deformation mode and compressive mechanical properties of Ti–10V–3Fe–3Al alloy, *Acta Mater.* 84 (2015) 124–135.
- [16] S. Hanada, O. Izumi, Correlation of tensile properties, deformation modes, and phase stability in commercial β -phase titanium alloys, *Metall. Trans. A* 18 (1987) 265–271.
- [17] X.H. Min, K. Tsuzaki, S. Emura, K. Tsuchiya, Enhancement of uniform elongation in high strength Ti–Mo based alloys by combination of deformation modes, *Mater. Sci. Eng. A* 528 (2011) 4569–4578.
- [18] X.H. Min, K. Tsuzaki, S. Emura, K. Tsuchiya, Heterogeneous twin formation and its effect on tensile properties in Ti–Mo based beta titanium alloys, *Mater. Sci. Eng. A* 554 (2012) 53–60.
- [19] M. Marteleur, F. Sun, T. Gloriant, P. Vermaut, P.J. Jacques, F. Prima, On the design of new β -metastable titanium alloys with improved work hardening rate thanks to simultaneous TRIP and TWIP effects, *Scr. Mater.* 66 (2012) 749–752.
- [20] F. Sun, J.Y. Zhang, M. Marteleur, T. Gloriant, P. Vermaut, D. Laillé, P. Castany, C. Curfs, P.J. Jacques, F. Prima, Investigation of early stage deformation mechanisms in a metastable β titanium alloy showing combined twinning-induced plasticity and transformation-induced plasticity effects, *Acta Mater.* 61 (2013) 6406–6417.
- [21] F. Sun, J.Y. Zhang, M. Marteleur, C. Brozek, E.F. Rauch, M. Veron, P. Vermaut, P.J. Jacques, F. Prima, A new titanium alloy with a combination of high strength, high strain hardening and improved ductility, *Scr. Mater.* 94 (2015) 17–20.
- [22] M.J. Blackburn, J.A. Feeny, Stress-induced transformations in Ti–Mo alloys, *J. Inst. Met.* 99 (1971) 132–134.
- [23] S.J. Wang, M.L. Sui, Y.T. Chen, Q.H. Lu, E. Ma, X.Y. Pei, Q.Z. Li, H.B. Hu,

- Microstructural fingerprints of phase transitions in shock-loaded iron, *Sci. Rep.* 3 (2013) 1086.
- [24] L.M. Dougherty, G.T. Gray III, E.K. Cerreta, R.J. McCabe, R.D. Field, J.F. Bingert, Rare twin linked to high-pressure phase transition in iron, *Scr. Mater.* 60 (2009) 772–775.
- [25] S. Hanada, O. Izumi, Transmission electron microscopic observations of mechanical twinning in metastable beta titanium alloys, *Metall. Trans. A* 17 (1986) 1409–1420.
- [26] S. Hanada, T. Yoshio, O. Izumi, Effect of plastic deformation modes on tensile properties of beta titanium alloys, *Trans. Jpn. Inst. Met.* 27 (1986) 496–503.
- [27] G. Carter, H.M. Flower, G.M. Pennock, D.R.F. West, The deformation characteristics of metastable β -phase in a Ti-15 wt % Mo alloy, *J. Mater. Sci.* 12 (1977) 2149–2153.
- [28] S. Hanada, M. Ozeki, O. Izumi, Deformation characteristics in β phase Ti-Nb alloys, *Metall. Trans. A* 16 (1985) 789–795.
- [29] T. Furuhashi, K. Kishimoto, T. Maki, Transmission electron-microscopy of $\{332\}$ $\langle 113 \rangle$ deformation twin in Ti-15V-3Cr-3Sn-3Al alloy, *Mater. Trans. JIM* 35 (1994) 843–850.
- [30] X. Zhao, M. Niinomi, M. Nakai, J. Hieda, T. Ishimoto, T. Nakano, Optimization of Cr content of metastable β -type Ti-Cr alloys with changeable Young's modulus for spinal fixation applications, *Acta Biomater.* 8 (2012) 2392–2400.
- [31] A.G. Crocker, Twinned martensite, *Acta Metall.* 10 (1962) 113–122.
- [32] T. Kawabata, S. Kawasaki, O. Izumi, Mechanical properties of TiNbTa single crystals at cryogenic temperatures, *Acta Mater.* 46 (1998) 2705–2715.
- [33] V.S. Litvinov, G.M. Ruskov, Twinning on the $\{332\}\langle 113 \rangle$ system in unstable beta titanium alloys, *Phys. Met. Metallogr.* 90 (2000) S96–S107.
- [34] P.G. Oberston, S. Ankem, Why twins do not grow at the speed of sound all the time, *Phys. Rev. Lett.* 95 (2005) 165501.
- [35] G.M. Ruskov, A.V. Litvinov, V.S. Litvinov, Deformation twinning of titanium beta-alloys of transition class, *Metal Sci. Heat Treat.* 48 (2006) 244–251.
- [36] H. Tobe, H.Y. Kim, T. Inamura, H. Hosoda, S. Miyazaki, Origin of $\{332\}$ twinning in metastable β -Ti alloys, *Acta Mater.* 64 (2014) 345–355.
- [37] C.C. Tasan, M. Diehl, D. Yan, C. Zambaldi, P. Shanthraj, F. Roters, D. Raabe, Integrated experimental–simulation analysis of stress and strain partitioning in multiphase alloys, *Acta Mater.* 81 (2014) 386–400.
- [38] C. Zambaldi, S. Zaeferrer, S.I. Wright, Characterization of order domains in γ -TiAl by orientation microscopy based on electron backscatter diffraction, *J. Appl. Crystallogr.* 42 (2009) 1092–1101.
- [39] A.P. Hammersley, S.O. Svensson, A. Thompson, Calibration and correction of spatial distortions in 2D detector systems, *Nucl. Instrum. Methods Phys. Res. Sect. A* 346 (1994) 312–321.
- [40] A. Devaraj, S. Nag, R. Srinivasan, R.E.A. Williams, S. Banerjee, R. Banerjee, H.L. Fraser, Experimental evidence of concurrent compositional and structural instabilities leading to ω precipitation in titanium–molybdenum alloys, *Acta Mater.* 60 (2012) 596–609.
- [41] E. Bertrand, P. Castany, I. Péron, T. Gloriant, Twinning system selection in a metastable β -titanium alloy by Schmid factor analysis, *Scr. Mater.* 64 (2011) 1110–1113.
- [42] B.A. Bilby, A.G. Crocker, The theory of the crystallography of deformation twinning, *Proc. R. Soc. Lond. A* 288 (1965) 240–255.
- [43] Y. Zhang, Z. Li, C. Esling, J. Muller, X. Zhao, L. Zuo, A general method to determine twinning elements, *J. Appl. Crystallogr.* 43 (2010) 1426–1430.
- [44] C.-X. Li, H.-B. Luo, Q.-M. Hu, R. Yang, F.-X. Yin, O. Umezawa, L. Vitos, Lattice parameters and relative stability of α'' phase in binary titanium alloys from first-principles calculations, *Solid State Commun.* 159 (2013) 70–75.
- [45] E.G. Obbard, Y.L. Hao, R.J. Talling, S.J. Li, Y.W. Zhang, D. Dye, R. Yang, The effect of oxygen on α'' martensite and superelasticity in Ti–24Nb–4Zr–8Sn, *Acta Mater.* 59 (2011) 112–125.
- [46] H.Y. Kim, Y. Ikehara, J.I. Kim, H. Hosoda, S. Miyazaki, Martensitic transformation, shape memory effect and superelasticity of Ti-Nb binary alloys, *Acta Mater.* 54 (2006) 2419–2429.
- [47] S. Kajiwara, T. Kikuchi, Reversible movement of the austenite–martensite interface and dislocation structures in reverse-transformed austenite in Fe-Ni-C alloys, *Philos. Mag.* 48 (1983) 509–526.
- [48] X.L. Wu, X.Z. Liao, S.G. Srinivasan, F. Zhou, E.J. Lavernia, R.Z. Valiev, Y.T. Zhu, New deformation twinning mechanism generates zero macroscopic strain in nanocrystalline metals, *Phys. Rev. Lett.* 100 (2008) 095701.
- [49] L. Liu, J. Wang, S.K. Gong, S.X. Mao, High resolution transmission electron microscope observation of zero-strain deformation twinning mechanisms in Ag, *Phys. Rev. Lett.* 106 (2011) 175504.
- [50] D.S. Lieberman, M.S. Wechsler, T.A. Read, Cubic to orthorhombic diffusionless phase change—experimental and theoretical studies of AuCd, *J. Appl. Phys.* 26 (1954) 473–484.
- [51] Y. Liang, H. Kato, M. Taya, T. Mori, Infinitesimal approach to the crystallography of martensitic transformation: application to Ni-Ti, *Scr. Mater.* 43 (2000) 535–540.
- [52] T. Inamura, J.I. Kim, H.Y. Kim, H. Hosoda, K. Wakashima, S. Miyazaki, Composition dependent crystallography of α'' -martensite in Ti–Nb-based β -titanium alloy, *Philos. Mag.* 87 (2007) 3325–3350.
- [53] Y.W. Chai, H.Y. Kim, H. Hosoda, S. Miyazaki, Interfacial defects in Ti–Nb shape memory alloys, *Acta Mater.* 56 (2008) 3088–3097.
- [54] J. Ma, I. Karaman, R.D. Noebe, High temperature shape memory alloys, *Int. Mater. Rev.* 55 (2010) 257–315.
- [55] M.Y. Gutkin, K.N. Mikaelyan, V.E. Verijenko, Heterogeneous nucleation of martensite near free surface, *Acta Mater.* 49 (2001) 3811–3819.
- [56] Y.U. Wang, Y.M. Jin, A.G. Khachaturyan, The effects of free surfaces on martensite microstructures: 3D phase field microelasticity simulation study, *Acta Mater.* 52 (2004) 1039–1050.
- [57] S. Kajiwara, T. Kikuchi, Dislocation structures produced by reverse martensitic transformation in a Cu-Zn alloy, *Acta Metall.* 30 (1982) 589–598.
- [58] L. Lu, X. Chen, X. Huang, K. Lu, Revealing the maximum strength in nano-twinning copper, *Science* 323 (2009) 607–610.